



**HAL**  
open science

## Osteogenic Effect of Fisetin Doping in Bioactive Glass/Poly(caprolactone) Hybrid Scaffolds

Henri Granel, Cédric Bossard, Anne-Margaux Collignon, Fabien Wauquier, Julie Lesieur, Gael Y Rochefort, Edouard Jallot, Jonathan Lao, Yohann Wittrant

► **To cite this version:**

Henri Granel, Cédric Bossard, Anne-Margaux Collignon, Fabien Wauquier, Julie Lesieur, et al.. Osteogenic Effect of Fisetin Doping in Bioactive Glass/Poly(caprolactone) Hybrid Scaffolds. ACS Omega, 2022, 7 (26), pp.22279-22290. 10.1021/acsomega.2c01109 . hal-03857797

**HAL Id: hal-03857797**

**<https://uca.hal.science/hal-03857797>**

Submitted on 17 Nov 2022

**HAL** is a multi-disciplinary open access archive for the deposit and dissemination of scientific research documents, whether they are published or not. The documents may come from teaching and research institutions in France or abroad, or from public or private research centers.

L'archive ouverte pluridisciplinaire **HAL**, est destinée au dépôt et à la diffusion de documents scientifiques de niveau recherche, publiés ou non, émanant des établissements d'enseignement et de recherche français ou étrangers, des laboratoires publics ou privés.



Distributed under a Creative Commons Attribution 4.0 International License

# Osteogenic Effect of Fisetin Doping in Bioactive Glass/Poly(caprolactone) Hybrid Scaffolds

Henri Granel, Cédric Bossard, Anne-Margaux Collignon, Fabien Wauquier, Julie Lesieur, Gael Y. Rochefort, Edouard Jallot, Jonathan Lao, and Yohann Wittrant\*



Cite This: *ACS Omega* 2022, 7, 22279–22290



Read Online

ACCESS |



Metrics & More



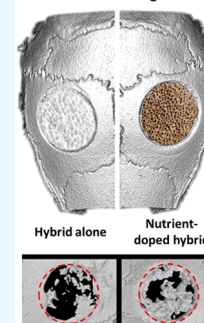
Article Recommendations



Supporting Information

**ABSTRACT:** Treating large bone defects or fragile patients may require enhancing the bone regeneration rate to overcome a weak contribution from the body. This work investigates the osteogenic potential of nutrient fisetin, a flavonoid found in fruits and vegetables, as a doping agent inside the structure of a SiO<sub>2</sub>–CaO bioactive glass–poly(caprolactone) (BG–PCL) hybrid scaffold. Embedded in the full mass of the BG–PCL hybrid during one-pot synthesis, we demonstrate fisetin to be delivered sustainably; the release follows a first-order kinetics with active fisetin concentration being delivered for more than 1 month (36 days). The biological effect of BG–PCL–fisetin-doped scaffolds (BG–PCL–Fis) has been highlighted by in vitro and in vivo studies. A positive impact is demonstrated on the adhesion and the differentiation of rat primary osteoblasts, without an adverse cytotoxic effect. Implantation in critical-size mouse calvaria defects shows bone remodeling characteristics and remarkable enhancement of bone regeneration for fisetin-doped scaffolds, with the regenerated bone volume being twofold that of nondoped scaffolds and fourfold that of a commercial trabecular bovine bone substitute. Such highly bioactive materials could stand as competitive alternative strategies involving biomaterials loaded with growth factors, the use of the latter being the subject of growing concerns.

Nutrient-doped hybrid bioglass for enhanced bone regeneration



## 1. INTRODUCTION

To address osteoarticular issues, the human body possesses natural healing mechanisms, but in the case of large bone defects or for vulnerable people, endogenous repair has to be assisted. Among the different biomaterials used to treat bone defects, bioceramics have been extensively studied and have exhibit satisfying biocompatibility with sometimes pro-osteogenic properties.<sup>1</sup> Bioceramics have continuously evolved from particles and monoliths to three-dimensional (3D) scaffolds that seem to be the most suitable solution for filling large bone defects.<sup>2</sup> Of special interest, bioactive glass (BG)-based biomaterials strongly bond to bone and their dissolution products (silicon species especially) stimulate osteogenic cells.<sup>1b,3</sup> BG is brittle, especially under the form of highly porous scaffolds, but it can be combined with a polymer to obtain a tougher material. In this light, promising sol–gel hybrid scaffolds combining silicates or BG and polymers including poly(caprolactone) (PCL), gelatin, poly(methylhydrosiloxane), and others have been proposed.<sup>4</sup> Unlike composites, the mixed organic and inorganic phases are expected to act as a single one above the nanoscale in hybrid materials. Besides, the degradation rate can be tailored depending on both the chosen polymer and the organic/inorganic ratio to ensure the ability of the implanted biomaterial to support the regeneration of tissues while remaining stable over time.

We reported in a previous work the in vivo performance of SiO<sub>2</sub>–CaO BG/PCL hybrid scaffolds, with almost a doubled

amount of regenerated bone volume compared to a commercial bovine xenograft used in orthopedics and periodontal procedures and yet acknowledged nearly as efficient as autograft standards.<sup>5</sup>

However, there is an ever-ongoing push to further increase the bone regeneration capacity through promotion of the bone cells' activity, which is of special interest for fragile patients whose bone remodeling capability can be limited as a result of age or health conditions. A further increase of the bone regeneration capabilities of such bone substitutes requires the addition of components with proangiogenesis or pro-osteogenesis abilities.

Among organic molecules used to increase osteogenesis, bone morphogenetic protein growth factors (BMPs) are widely documented, and their efficiency is well established in vitro, in vivo, and at a clinical level, most notably for craniofacial surgeries.<sup>6</sup> However, their use now raises serious concerns regarding their adverse effects and long-term safety issues. For instance, doping with BMPs has been associated with a higher risk of cancer, ectopic bone formation, edema, osteolysis, and pseudarthrosis.<sup>6a,7</sup> On the other hand, nutritional strategies

Received: February 24, 2022

Accepted: June 7, 2022

Published: June 21, 2022



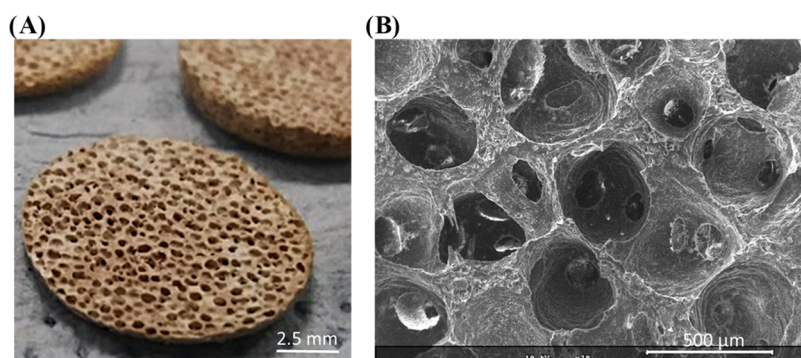


**Figure 1.** (A) Optical view of BG–PCL–Fis scaffolds showing their initial color and porosity. (B) Scanning electron microscopy (SEM) image at  $\times 70$  magnification (the scale bar is  $500\ \mu\text{m}$ ).

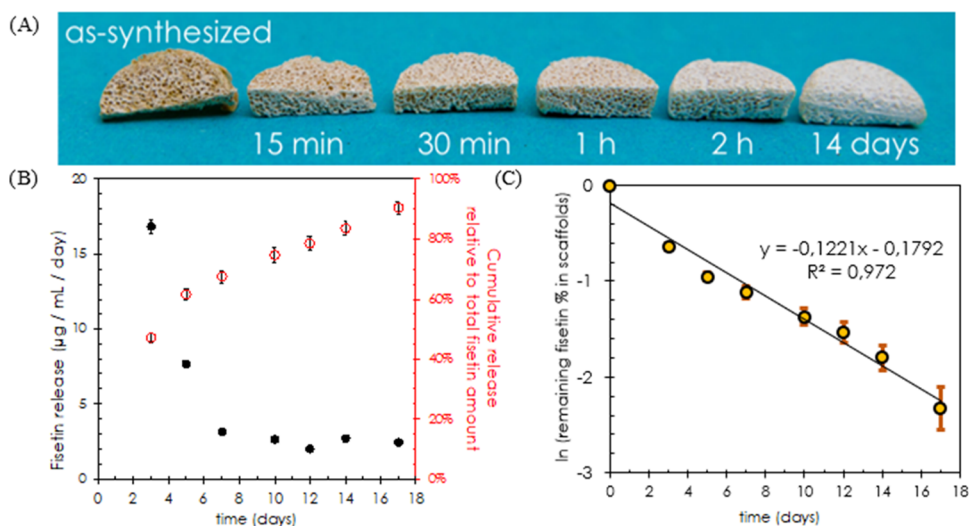


**Figure 2.** (A) Optical view of BG–PCL–Fis scaffolds as a function of the immersion time in the biological medium. (B) Evolution of fisetin release from BG–PCL–Fis scaffolds normalized per day of immersion in the biological medium in the presence of rat primary osteoblast (RPO) cells (black dots) and the corresponding cumulative fisetin release relative to the total fisetin amount incorporated in the scaffold (empty red dots). (C) Napierian logarithm of the unreleased fraction of fisetin (%) versus time (days).

based on a variety of organic compounds naturally derived from vegetables, plants, or fruits can be safely used to promote osteogenesis, prevent bone loss, and stimulate cell-driven mineralization. Dietary polyphenols seem to be among the most promising natural molecules with proven benefits for bones both *in vivo* and clinically and have deserved particular attention in nutritional strategies for skeletal and bone health.<sup>8</sup>

Accordingly, designing bone substitutes as delivery systems for these natural agents is of great interest and has recently been discussed in the literature.<sup>9</sup> A few candidates have been successfully tested *in vitro* and/or *in vivo* including vitamin-, polyphenol-, tannin-, or protein (casein)-based approaches.<sup>9c,10</sup> Furthermore, ROS-responsive biomaterials have been identified as a type of promising therapeutic opportunity to alleviate oxidative stress and promote bone formation.<sup>11</sup>

In previous studies, we demonstrated that fisetin (3,3',4',7-tetrahydroxyflavone), a flavonoid found in various fruits and vegetables such as strawberry, apple, persimmon, grape, onion, and cucumber, was able to limit the osteoporosis onset in a mouse model of estrogen deficiency.<sup>12</sup> Furthermore, we demonstrated that flavonoid fisetin promotes osteoblasts differentiation through Runx2 transcriptional activity and further supports collagen 1 synthesis and subsequent bone mineralization.<sup>12,13</sup> Such pro-osteogenic properties were

recently further investigated in a zebrafish model of vertebral formation. In this model, the authors showed that fisetin-induced osteogenic effects occurred through phosphorylation of glycogen synthase kinase-3 $\beta$  (GSK-3 $\beta$ ) and subsequent release and nuclear translocation of  $\beta$ -catenin.<sup>14</sup> Besides, in contrast to BMPs, fisetin has been reported for its benefit in bone tumorigenesis prevention including inhibition of migration and invasion and promotion of apoptosis of human osteosarcoma cells.<sup>15</sup>

In this light, we wondered whether and how such an organic component could be of interest for doping BG–PCL hybrids in an attempt to favor osteoblasts differentiation *in situ*.

Organic compounds are sensitive to high temperatures. Consistently, it is worth noting that the sol–gel route, we used to synthesize silicate hybrids, is conducted under mild conditions and at room temperature, opening up new possibilities for doping with such compounds. Very recently, we succeeded in doping poly(caprolactone)–silica hybrids with rifampicin for tailored therapeutic release of antibiotics in the treatment of osteomyelitis.<sup>16</sup> Thus, our sol–gel process allows the introduction of fisetin *in situ* during the synthesis of BG–PCL hybrids. This doping-in-the-bulk technique contrasts with the usual adsorption techniques employed for organic loading, which commonly results in a nonsustainable release

with an immediate burst of the loaded agent and limited long-term potential.<sup>17</sup> The aim of the present work was both to investigate the feasibility of such a full-mass nutrient-based doping strategy regarding its release and the sustainability of this release and to decipher whether fisetin, within the hybrid, could retain a pro-osteogenic activity when released. Hence, BG–PCL hybrid scaffolds were doped with fisetin by one-pot synthesis; fisetin delivery from hybrids in the presence of cells was investigated, while its effect on the viability, adhesion, and differentiation of primary osteoblastic cells was assessed. Finally, BG–PCL–fisetin (BG–PCL–Fis) hybrid scaffolds were implanted *in vivo* in a challenging mouse model of critical-size calvaria defect and their performance was compared to that of undoped BG–PCL hybrids.

## 2. RESULTS

**2.1. BG–PCL–Fis Scaffold Observation and Fisetin Release.** The porous leaching technique yields highly porous structures (Figure 1).<sup>4c</sup> In a previous work, we measured the porosity to reach  $75 \pm 2\%$  by X-ray microtomography.<sup>4a,18</sup> Such an open structure should favor fluid penetration and promote reaction exchange and fisetin delivery, but the question remains open regarding release sustainability.

A significant change in the color of BG–PCL–Fis scaffolds is observed during their immersion in the biological medium, turning from the initial orange–brown of fisetin scaffolds to white, the standard color of undoped BG–PCL scaffolds, after a few days of soaking (Figure 2). This color change is related to the release of fisetin (Figure 2B). The 3 day preincubation step leads first to quick delivery of fisetin in a-MEM, reaching  $50.5 \mu\text{g}/\text{mL}$  concentration after 3 days, equivalent to nearly half (47%) of the total amount of fisetin loaded in the scaffolds and a  $16.8 \mu\text{g}/\text{mL}/\text{day}$  average release. After preincubation, the BG–PCL–Fis scaffolds are incubated with rat primary osteoblast (RPO) cells, i.e., from day 3 to day 17. The daily fisetin release decreases and then stabilizes at  $2\text{--}3 \mu\text{g}/\text{mL}/\text{day}$  from day 7 to day 17. A 90% fisetin release is reached after 17 days of soaking in the biological medium.

**2.2. RPO Viability in the Presence of BG–PCL–Fis or BG–PCL Dissolution Products.** To ensure that the biological activity would not be impeded by any cytotoxic or cytostatic effects, we first checked the influence of dissolution products of the hybrids on RPO cell proliferation and viability (Figure 3). Although fisetin doping showed a weak enhancement of the cell viability (+12% versus the cell layer control and +9% versus BG–PCL), there was no significant statistical difference between the experimental conditions. This suggests that the growth and proliferation of cells are not impeded by the dissolution products of BG–PCL and BG–PCL–Fis.

**2.3. Fisetin Doping of the Hybrid Favors Cell Adhesion and Spreading.** Rat primary osteoblasts (RPOs) were cultured on BG–PCL and BG–PCL–Fis disks and investigated by scanning electron microscopy (SEM) (Figure 4). Human cortical bone (HCB) slices were used as a control. Adhesion of cells was observed for all conditions, with protruding filopodia; remarkably, the extent of cell spreading increased in the following order HCB < BG–PCL < BG–PCL–Fis, suggesting the effect of BG–PCL on cell growth that can be further enhanced by the presence of fisetin.

**2.4. Fisetin Doping of the Hybrid Enhances Its Osteogenic Potential.** To evaluate the biological relevance of our doping strategy, RPOs were grown for 7–14 days on BG–PCL or BG–PCL–Fis scaffolds and alkaline phosphatase

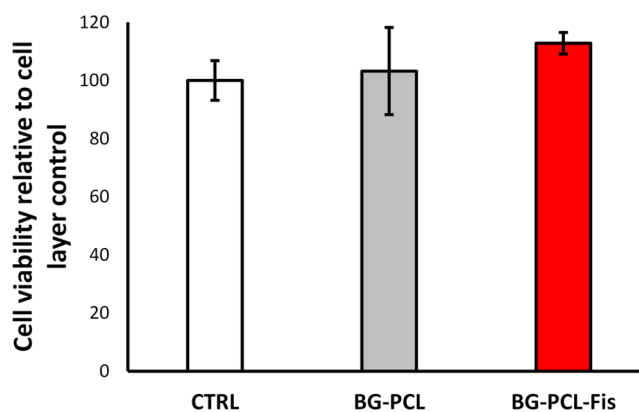


**Figure 3.** RPO viability (XTT-based assay; brand name) after 7 days of culture. The mitochondrial activity is expressed as a percentage of the cell layer control condition ( $n = 6$ ). No significant difference is observed.

activity (ALP) was determined as a marker of the osteoblastic function (Figure 5). As soon as 7 days of culture, ALP activity was significantly enhanced by the presence of fisetin polyphenol (+463% compared to BG–PCL after 7 days). Remarkably, ALP activity in BG–PCL–Fis on day 7 was similar to that in BG–PCL on day 14. The stimulation of ALP activity by fisetin was confirmed and considerably strengthened after 2 weeks.

To determine how fisetin doping affects osteoblast differentiation, Runx2 transcription factor and type 1 collagen (COL1) protein levels were analyzed by western blotting (Figure 6). RPOs were cultured for 7 and 14 days either on BG–PCL or BG–PCL–Fis scaffolds. As shown by blots and relative quantifications, BG–PCL–Fis increased COL1 and Runx2 expression levels compared to undoped BG–PCL. The difference was statistically significant for Runx2 on day 14.

**2.5. Fisetin Doping Strategy Enhances Bone Regeneration *In Vivo*.** BG–PCL and BG–PCL–Fis were implanted in critical-size mouse calvaria defects and the bone regeneration was investigated and quantified using micro-computed tomography (CT) (Figure 7). Postoperative CT scans demonstrated that BG–PCL and BG–PCL–Fis scaffolds are transparent to X-rays and thus invisible in Figure 7A (BG–PCL D0 and BG–PCL–Fis D0) as a result of their low density. This allowed however to easily detect the formation of new bone inside the defects. After 30 days of implantation, SHAM (control left empty) showed a limited  $10 \pm 1\%$  (Figure 7B) amount of bone regenerated, with a remodeling process typically coming from the periphery of the defect (Figure 7A, Ctrl D30). In contrast, for defects filled with BG–PCL, a significantly higher bone volume ( $23 \pm 5\%$ ) was measured (Figure 7B). For BG–PCL–Fis, bone repair reached  $33 \pm 5\%$  (Figure 7B). At the end of the 90 day trial,  $13 \pm 1\%$  of bone was regenerated in sham-operated animals, a value below the upper limit (<15%) commonly admitted for a defect to be considered of critical size, thus validating the model. Filling defects with undoped BG–PCL scaffolds led to an increased new bone formation with  $32 \pm 4\%$  BV/TV (bone volume fraction) of the defect repaired (Figure 7B). Remarkably, for BG–PCL–Fis, new bone formation extended to the whole defect with the highest regenerated BV/TV ratio ( $55 \pm 7\%$ ) of the initial defect filled with a new bone after 90 days of implantation.

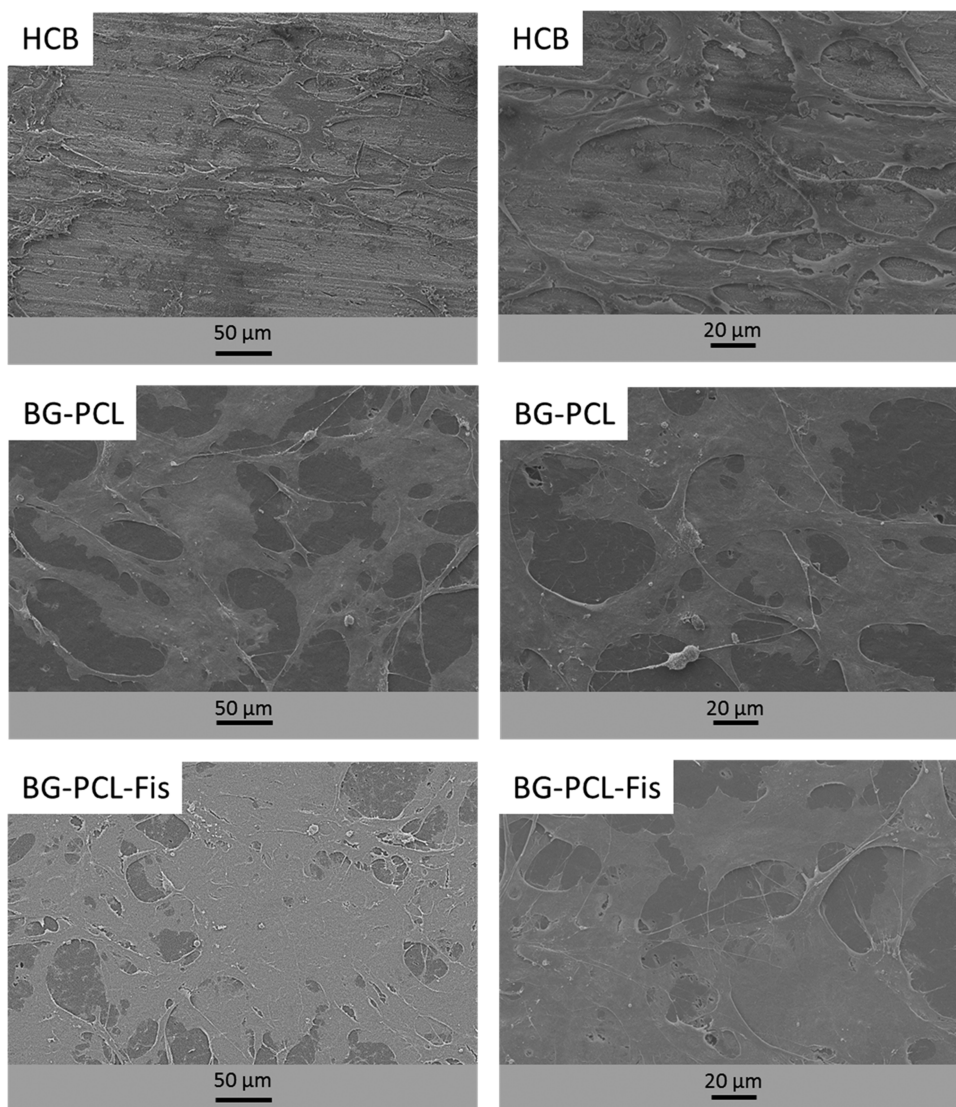


**Figure 4.** SEM pictures of RPO cultured on flat human cortical bone (HCB) slices, flat BG-PCL, and BG-PCL-Fis disks ( $n = 3$ ).

**2.6. New Bone Formation Is Driven by Active Cellular Remodeling.** Histological analyses were conducted to further elucidate the cellular mechanisms involved in the bone regeneration process following BG-PCL and BG-PCL-Fis implantation in calvaria defects (Figure 8). Bone remodeling is evidenced by a modified Masson–Goldner trichrome staining, resulting in collagen fibers being stained in green.

Consistent with micro-CT data, new bone formation (appearing as dark green regions and labeled as NB in Figure 8) is demonstrated for BG-PCL implanted calvaria (Figure 8A). Interestingly, when BG-PCL is doped with 1 wt % fisetin, green staining appears darker and pink staining becomes more frequent and pronounced (Figure 8B), corresponding to higher collagen synthesis and osteoid formation, thus supporting faster bone growth for BG-PCL-Fis scaffolds.

Magnification attests to the presence of osteoblast and osteoclast remodeling cells (Figure 8A,B). In addition, the cellular organization is further highlighted by ALP (alkaline phosphatase) purple staining (Figures 8C and 7D) and TRAP (tartrate-resistant acid phosphatase) red staining (indicated by \*; Figure 8E,F).

### 3. DISCUSSION

In biomaterial engineering, and especially when designing bone substitutes biomaterials, the delivery of drugs or active compounds often relies on surface adsorption or surface immobilization strategies.<sup>1b,19</sup> Controlling the release profile and promoting a sustained release over time are common issues. Here, we took advantage of the soft chemistry route enabled by the sol-gel process to perform a bulk loading of fisetin, a thermally sensitive flavonoid, in one-pot synthesis of BG-PCL-Fis hybrid materials. This “full-mass” doping strategy was expected to ensure a long-term release of the compound, the doped material being the reservoir of the active dopant.

From the in vitro fisetin release assays (Figure 2B), it is observed that the concentration of fisetin delivered decreases over time. This behavior can be a signature of first-order kinetics, for which the release of a compound is proportional to the remaining amount in the reservoir material. This type of kinetics is often observed for soluble agents incorporated in a porous matrix.<sup>20</sup> The assumption of this model is that the change in fisetin concentration  $dF$  is proportional to the amount of remaining fisetin  $F$  in the reservoir material and the

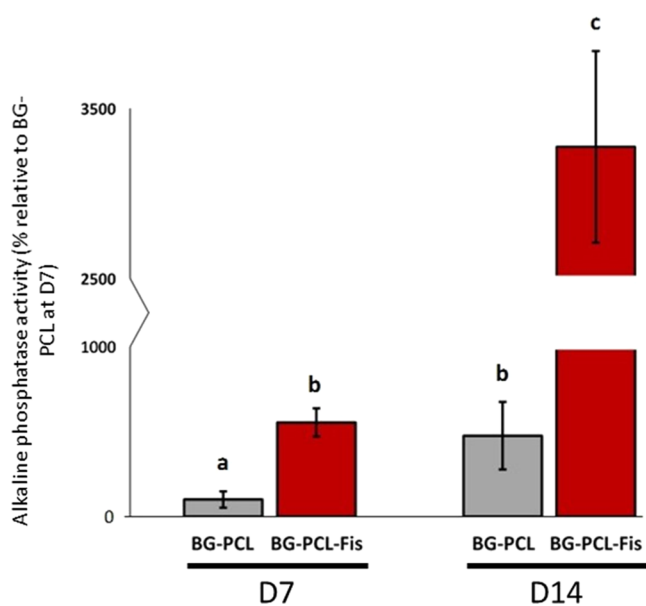


**Figure 5.** ALP activity of RPOs cultured inside BG-PCL and BG-PCL-Fis scaffolds ( $n = 3$ ), measured after 7 and 14 days of culture. Groups with significant differences ( $p < 0.05$ ) are indicated with different letters (a–c). Groups with no significant statistical difference from each other share the same letter.

interval of time  $dt$ :  $dF = -k.F.dt$ . It is negative since it corresponds to a release and the proportional constant  $k$  corresponds to the first-order rate constant. Integration of this differential equation leads to the instant remaining fisetin concentration in BG-PCL-Fis scaffolds:  $F(t) = F_0.exp(-kt)$ , with  $F_0$  being the initial amount of fisetin incorporated. Figure 2C shows the adequation of the first-order kinetics model with our experimental data, with a coefficient of determination  $R^2 = 0.972$  (Figure 2C). Interestingly, from this model, we can deduce  $-dF/dt = k.F$ , which represents the instantaneous rate of fisetin delivery. In a previous work, we found that fisetin promoted osteoblast activity for delivered concentrations ranging between 1 and 10  $\mu M$  per period of 2 days, corresponding to daily fisetin delivery rates of 0.143–1.43  $\mu g/mL/day$ .<sup>15</sup> If we retain the lowest of these values as the

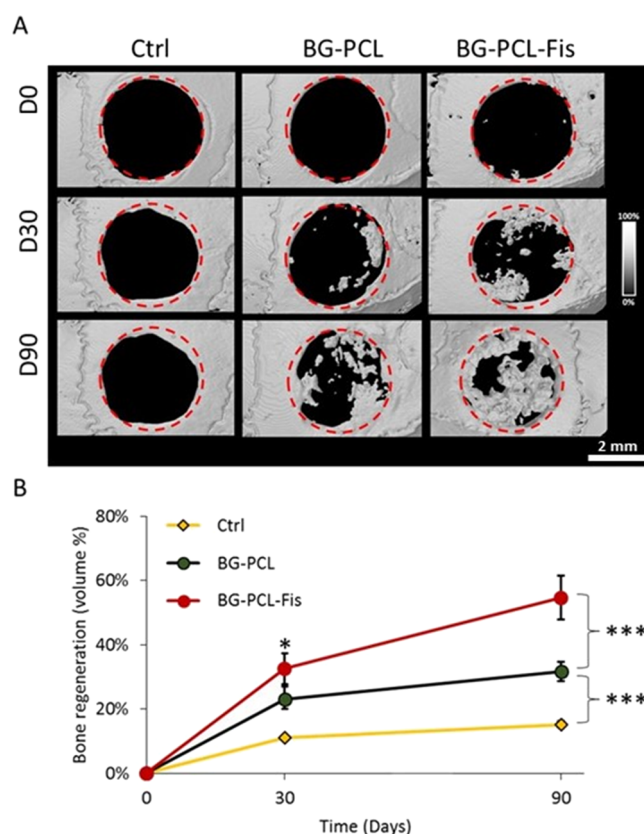


**Figure 7.** Micro-CT analysis of the different scaffolds (BG-PCL, BG-PCL-Fis) implanted in critical-size mice calvaria defects compared to an empty (sham) control defect at 0, 30, and 90 days ( $n = 8$ ). (A) Representative example of visual rendering of bone regeneration in each group. Note that BG-PCL and BG-PCL-Fis scaffolds are radiolucent. (B) Quantification of bone regeneration ( $n = 8$  per group) as % of the “new tissue” volumetric fraction over the volume of the defect. (\*\*\*) stands for  $p < 0.001$ . Videos of corresponding 3D files are available as [Supporting Data](#).

minimum concentration to be delivered daily to achieve a beneficial effect on bone cells and osteogenesis, by solving  $-dF/dt = 0.143$ , we can infer that the delivery rate  $k.F$  will not fall under the minimum required before the time  $t = 36.6$  days,

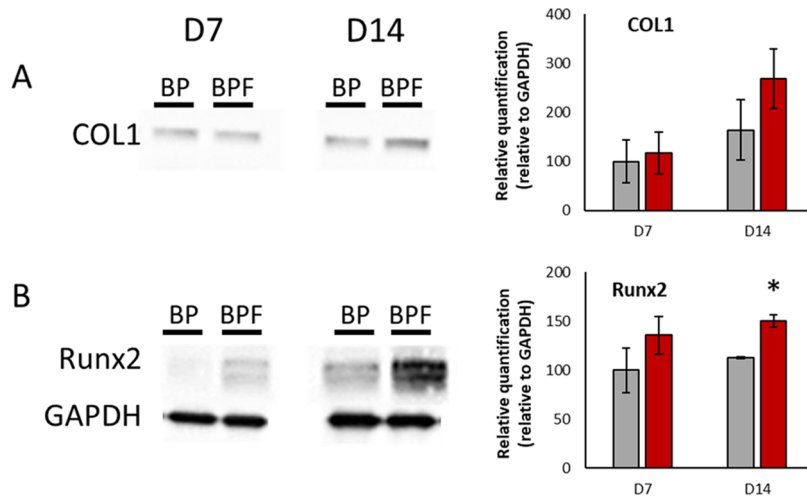


**Figure 6.** (A) COL1 and (B) Runx2 western blots on proteins extracted from RPO after 7 and 14 days of culture inside BG-PCL (BP) or BG-PCL-Fis (BPF) scaffolds and relative quantification as % of BG-PCL (BP) on day 7 ( $n = 3$ ). \* $p < 0.05$ .

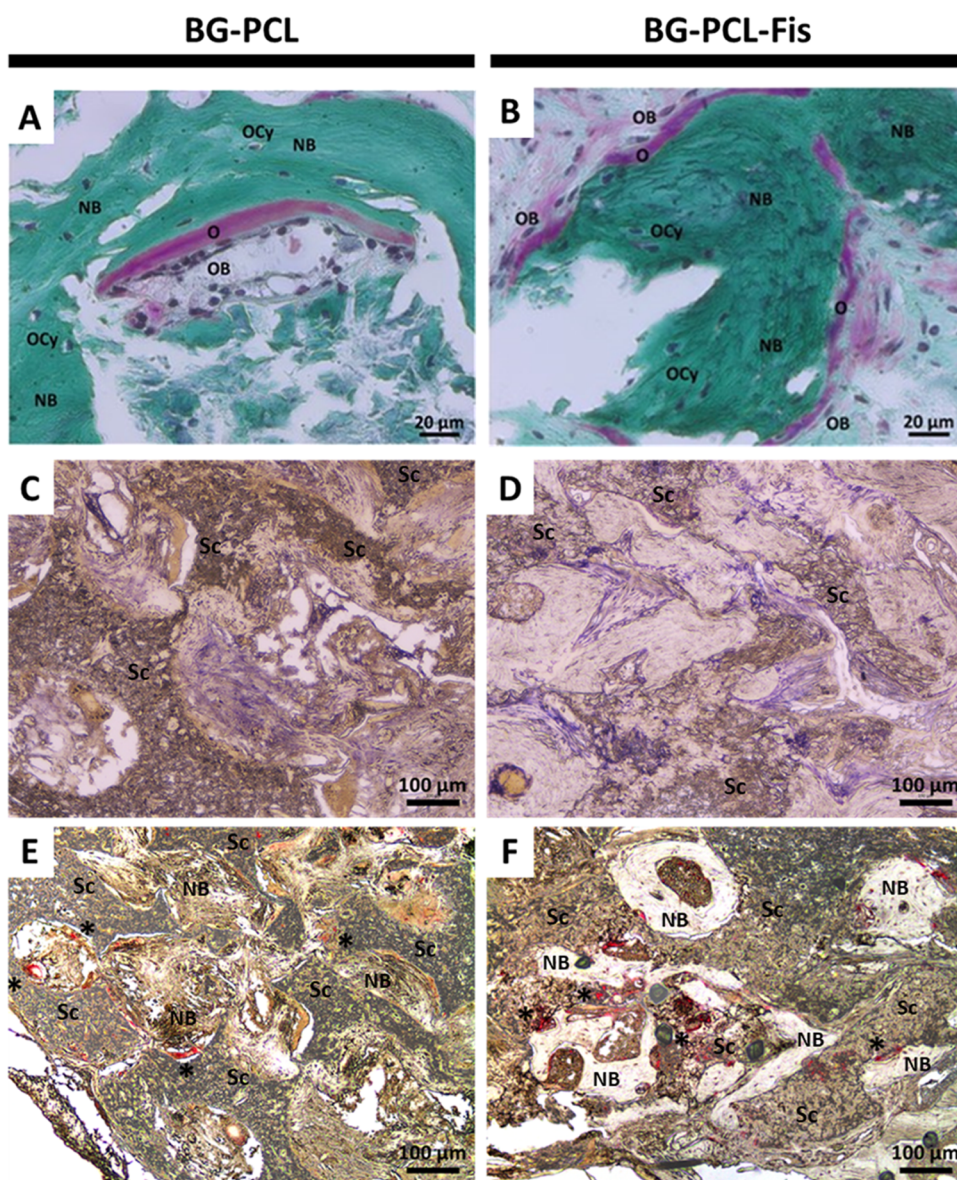


**Figure 8.** Histological staining of frontal demineralized tissue sections of critical-size calvaria defects after 90 days of implantation of BG–PCL or BG–PCL–Fis scaffolds. (A, B) Modified Masson–Goldner trichrome allows the observation of collagen (green), osteoid tissues (pink), and bone cell nuclei (dark purple) (NB, new bone; Sc, remaining scaffold; O, osteoid; OB, osteoblast; OCy, osteocyte). Bone cells driving the tissue remodeling process were also highlighted by enzymatic staining of ALP (purple) (C, D) or TRAP (red\*) (E, F).

corresponding to a total 99% cumulative fisetin release. Therefore, one can reasonably assume that a sustainable release is achieved over more than 1 month with an active concentration of fisetin delivered to stimulate bone cells and promote mineralization and bone regeneration.

From the *in vitro* assays, it is demonstrated that BG–PCL–Fis scaffolds neither exert cytotoxic nor proliferative effects on RPO but rather favored their adhesion, spreading, and activity. These positive influences on osteoblast behavior were confirmed by *in vivo* experiments showing a major enhancement of bone regeneration, with BV/TV values measured for BG–PCL–Fis being nearly twice those for undoped BG–PCL. Interestingly, in a previous work, we already demonstrated a twofold enhancement of new bone formation of BG–PCL over a bovine trabecular bone scaffold. Accordingly, doping with fisetin may improve by 4 times the bone regeneration obtained with a commercial bovine xenograft used in

orthopedics and periodontal procedures, yet acknowledged nearly as efficient as autograft standards.<sup>5</sup>

This remarkable result is supported by the development of functional bone modeling units as evidenced by the histological observation of stained explanted sections of the bone defect area. The superior osteogenic property demonstrated by BG–PCL–Fis scaffolds can obviously be attributed to the presence of fisetin in the scaffolds together with its sustained delivery. Regarding the mechanisms of action, in a previous study, we demonstrated that fisetin promotes both alkaline phosphatase activity and mineralization process by upregulating the Runx2 protein level and transcriptional activity.<sup>13</sup> This is consistent with the present results: the Runx2 protein level was also upregulated for BG–PCL–Fis. Moreover, we observed an increased expression of type 1 collagen protein, a transcriptional target of Runx2 for BG–PCL–Fis scaffolds. These results nicely agree with our

previous work and support that the fisetin released by the biomaterial is fully functional and enhances osteoblast differentiation and activity at least through Runx2.

Finally, it is of the deepest interest to compare the performance of BG–PCL–Fis hybrid scaffolds with various BMP-loaded biomaterials evaluated using the same surgically challenging model based on the calvaria critical-size defect. Indeed the healing of long bone is known to be much faster than that of flat bone, with, e.g., the tibial bone regeneration rate being reported to be twofold faster than that of calvaria bone.<sup>21</sup> Huang et al. implanted mice with poly(L-lactic acid) (PLLA) nanosheets loaded with BMP-2 in 3.5 mm diameter critical-size defects—the exact same defect dimension used in our study. The BMP-2-loaded PLLA induced a 1.5 mm<sup>3</sup> regenerated volume after 4 weeks, increasing up to 2.2 mm<sup>3</sup> after 8 weeks; although the defect thickness was not mentioned since these were full-thickness calvaria defects and the mice calvaria is less than 1 mm thick, it corresponds to regenerated BV/TV values of approximately 15–40%.<sup>21,22</sup> Similarly, Gronowicz et al. investigated mineralized collagen/hydroxyapatite scaffolds loaded with BMP-2 and fibroblast growth factor FGF-2 in a 3.5 mm diameter critical mice calvaria defect: they reported a maximum BV/TV equivalent to 15% after 6 weeks of implantation.<sup>23</sup> PLGA microspheres loaded with either BMP-2, metalloproteinase MMP10, or a combination of both resulted in 20–50% BV/TV after 4 weeks in a 4 mm mice calvaria defect.<sup>24</sup> Fibrin scaffolds loaded with BMP-2 implanted in noncritical calvaria mice defects (2.5 mm) exhibited a regeneration rate of around 20% BV/TV after 4 weeks (compared to 3% for undoped fibrin materials).<sup>25</sup> Overall, compared to our 33 and 55% regenerated BV/TV after 4 and 12 weeks, respectively, our data strongly supports the relevance of using fisetin as an alternative to growth factors to enhance the osteogenic potential of bone substitutes.

A fair comparison with other models of calvaria defects is delicate but remains instructive. The 13–93 bioactive glass (no BMP-loaded) scaffolds implanted in a noncritical (less than 8 mm) rat calvaria defect yielded a maximum of 30% regenerated BV/TV after 12 weeks.<sup>22</sup> PLGA scaffolds loaded with 240 ng/mm<sup>3</sup> BMP-2 allowed a 60% BV/TV regeneration in a 5 mm noncritical rat calvaria defect after 12 weeks.<sup>25</sup> Gelatin sponge constructs harvested with adipose stem cells expressing BMP-2 or chondrogenic TGF- $\beta$ 3 factors led to 20% and 60% BV/TV after 4 weeks and 12 weeks, respectively, in noncritical 8 mm rabbit calvaria defects.<sup>26</sup> Even against the more complex constructs involving stem cells, BG–PCL scaffolds doped with 1 wt % fisetin seem therefore to remain competitive, with the bone regeneration rate among the highest reported.

#### 4. CONCLUSIONS

In this study, we demonstrated for the first time the feasibility and the biological relevance of an innovative full-mass organic doped hybrid synthesis using an original pro-osteogenic nutrient-based strategy. Such doping-in-the-bulk method led to a sustained release of fisetin for more than 2 weeks with active concentration expected to be delivered for more than 1 month in vitro. Furthermore, our data demonstrate that the osteogenic properties of the flavonoid fisetin were preserved throughout the synthesis of the hybrid scaffolds as confirmed by a remarkable enhancement of bone regeneration properties of fisetin-doped BG/PCL hybrids. This doping strategy involving nutrients is a promising alternative to growth factors for treating the most difficult clinical cases or healing

vulnerable patients. This study also paves the way for the incorporation of other polyphenols or nutrient compounds known for their osteogenic, angiogenic, or antibacterial properties.

#### 5. EXPERIMENTAL SECTION/METHODS

**5.1. Synthesis of Hybrid Scaffolds.** Material composition consisted of 30 wt % SiO<sub>2</sub>[75 wt %]–CaO[25 wt %] BG and 70 wt % PCL (Mn = 80 k) for undoped hybrids (BG–PCL) or 69 wt % PCL and 1 wt % fisetin for fisetin-doped hybrids (BG–PCL–Fis). The materials were derived from sol–gel syntheses following the steps detailed in Bossard et al.<sup>4a</sup> Briefly, the sol–gel process was first initiated through an acid-catalyzed route involving the hydrolysis of tetraethyl orthosilicate (TEOS) (99% purity, Aldrich) in ethanol (absolute, Aldrich) acidified with HCl (2 M, Aldrich) (TEOS/H<sub>2</sub>O/HCl/ethanol molar ratio = 1:2:0.07:3.7). A solution of calcium (calcium ethoxide powder, 95% purity, Gelest, dispersed in ethanol) was introduced after 30 min in the TEOS sol in a stoichiometric proportion (targeted BG nominal composition of 75 wt % SiO<sub>2</sub> and 25 wt % CaO). In parallel, a 18.2 w/v % solution of PCL (Mn = 80,000 g mol<sup>-1</sup>, Aldrich) in tetrahydrofuran solvent (THF) was prepared. For fisetin-doped hybrids, fisetin was introduced in the PCL–THF solution after the completion of PCL dissolution. The TEOS–calcium ethoxide solution and the PCL solution were mixed together right before gelation of the TEOS–calcium ethoxide solution (which can typically occur between 30 and 2 h). The resulting hybrid solution was stirred for 15 min, then placed in an ultrasonic bath for 30 min, and stirred for another 1 h for homogenization and further condensation. Afterward, the hybrid sol was poured on a stack of paraffin microspheres that were used as a template to generate porous scaffolds (porogen leaching method). The paraffin microspheres were obtained by performing an oil-in-water emulsion following a process described in Ma et al.<sup>27</sup> The microspheres were then sieved to sort out the 400–600  $\mu$ m fraction, which was poured into 10 mm polyethylene molds and heated at 50 °C for 1 h to provoke the bridging of the spheres. To help the hybrid solution infiltrate the stack of paraffin microspheres, the molds were placed in a centrifuge (6000 rpm). The hybrid sol infiltrated in the stack of spheres was left as in the molds completely opened for solvent evaporation and subsequent gelation of the hybrid sol for 72 h at RTP. Once the structures dried, cyclohexane baths allowed the dissolution of the paraffine porogen spheres, leaving a network of spheric and interconnected macropores. A final washing step in absolute ethanol for 24 h was performed for removal of residual cyclohexane. Remarkably, this procedure yielded porous hybrid scaffolds that are covered by a dense cortical layer of hybrid material at their top. Here, this top cortical layer was 3  $\mu$ m thick.

**5.2. Scanning Electron Microscopy (SEM).** The macroporous structure of BG–PCL–Fis was observed with an SH-3000 SEM (Hirox) operating at 10 keV; prior to analysis, the samples were carbon-coated.

**5.3. Primary Cell Isolation.** As described previously, rat primary osteoblast (RPO) cells were enzymatically isolated from fetal Wistar rat calvaria.<sup>28</sup> Briefly, explants were digested in a solution of  $\alpha$ -MEM, 1% penicillin/streptomycin (p/s), collagenase IA (0.1%), dispase II (0.2%) at 37 °C and incubated for 15 min at 37 °C four times. Cells from all of the explants were pooled and plated at a density of 10,000 cells/cm<sup>2</sup> in 225 cm<sup>2</sup> tissue culture dishes. Cells were cultured until

80% confluency was reached in  $\alpha$ -MEM medium supplemented with 10% fetal bovine serum (FBS) and 1% p/s in a controlled atmosphere (90% hygrometry, 5% CO<sub>2</sub>, 95% air, and 37 °C). Afterward, cells were collected and frozen in liquid nitrogen in 20% FBS, 7% dimethyl sulfoxide, and 73%  $\alpha$ -MEM.

**5.4. Primary Cell Cultures.** Scaffolds were glued to the bottom of wells in 12-well-plates to culture RPO directly inside BG–PCL and BG–PCL–Fis scaffolds (scaffolds diameter: 10 mm; height 2 mm), BG–PCL and BG–PCL–Fis flat disks (obtained by flattening scaffolds in a manual hydraulic press), and on slices of human cortical bone (kindly provided by OST Développement, Clermont-Ferrand). Cell culture wells were filled with 2 mL of  $\alpha$ -MEM medium and placed under vacuum for 72 h to remove air from scaffolds and avoid exposing the cells to the immediate burst of ions that occurs just after BG-based scaffold immersion according to Radin et al.<sup>29</sup> Then, RPOs were added on the material in a dropwise manner to reach a density of 100,000 cells per material. After seeding, scaffolds were left for 40 min at 37 °C (5% CO<sub>2</sub> and 90% hygrometry) for cell adhesion. The volumes of culture medium were then gently completed up to 2 mL with culture medium. Cells were grown inside the scaffolds under gentle orbital agitation while no agitation was applied to cells grown on the surface of the flat disks and on slices of human cortical bone. Indeed, dynamic conditions were required for 3D cell culture. A gradient in the concentration of oxygen was usually observed inside 3D structures under static conditions leading to deleterious cell behavior at the center of scaffolds.<sup>30</sup> The orbital speed was set at 10 rpm and with a 12° slot according to Perez et al., who highlighted better cell adhesion to the support with equivalent low agitation speed.<sup>31</sup> Media were replaced every 2 days.

**5.5. Cell Viability Assays.** RPOs were seeded on a 12-well plate (density: 10,000 cells/cm<sup>2</sup>) and grown for 7 days. To observe the impact of dissolution products on cell behavior, scaffolds were deposited in inserts equipped with a porous membrane [(pore size: 8  $\mu$ m) (Falcon)]. Then, inserts were placed in dedicated cell culture well plates. Cell viability was measured using the XTT-based method [cell viability/proliferation kit II (Sigma-Aldrich)] according to supplier's instructions. Accordingly, the optical density (OD) was measured at 450 nm.

**5.6. Cell Adhesion Assays.** Cells were grown on BG–PCL, BG–PCL–Fis disks, or human cortical bone slices for 12 h. Samples were fixed during 1 h with a 3% glutaraldehyde and 0.2 M sodium cacodylate buffer solution (pH 7.4). Samples were then washed three times in cacodylate buffer for 10 min each. Samples were then dehydrated with three gradual baths of ethanol (70, 95, and 100%) for 10 min each. A final treatment with hexamethyldisilazane baths (HMDS, Delta Microscopies) was applied. Samples were dried overnight, coated using a sputter coater (Jeol JFC-1300), and analyzed by SEM at 5 keV (Jeol 6060-LV).

**5.7. Alkaline Phosphatase Activity Assays.** Enzymatic alkaline phosphatase (ALP) activity was measured after 7 and 14 days of culture on protein extracts from cells cultured inside the scaffolds. Briefly, cells were rinsed with ice-cold PBS and cells were lysed with NP40 lysis buffer. Lysates were then incubated in the assay buffer [40 mM *p*-nitrophenyl phosphate (Sigma-Aldrich), alkaline assay buffer (Abcam)]. The production of *p*-nitrophenol was determined by spectroscopy (405 nm) at 37 °C and expressed as the mean OD per minute.

GAPDH expression obtained by immunoassay was used to normalize results.

**5.8. Fisetin Release Assays in the Presence of RPO.** BG–PCL–Fis scaffolds (20 mg, cylindrical shape with 10 mm diameter and 2 mm height) ( $n = 6$ ) were first preincubated for 3 days in 2 mL of  $\alpha$ -MEM containing 1% p/s (10 mg of scaffolds/mL of medium). After this 3 day preincubation step, the media was removed for analysis and replaced by 2 mL of a solution consisting of 89 vol %  $\alpha$ -MEM–10 vol % SVF–1 vol % p/s, and RPOs were seeded on the scaffolds as described above. Incubation media were renewed and analyzed on days 2, 4, 7, 9, 11, and 14 (day 0 being referred to as the end of the preincubation step). All experiments were performed in triplicate. Each time the biological medium was meant to be changed (after the initial 3 day preincubation period and on days 2, 4, 7, 9, 11, and 14 when renewing cell culture media), the supernatant liquid was carefully and entirely collected using a transfer pipette and then filtered using a millipore filter. Fisetin release from biomaterial was determined by spectrophotometry measuring the absorbance of the solutions at the absorbance peak at 336 nm. For calibration, two ranges of fisetin standard solutions were prepared in either  $\alpha$ -MEM-p/s (used for dosing the preincubation media) or 89 vol %  $\alpha$ -MEM–10 vol % SVF–1 vol % p/s (used for dosing the cell incubation media). For each range, a 50  $\mu$ g/mL stock solution was prepared and then diluted to obtain five different fisetin standard solutions with the following concentrations: 1.56, 3.13, 6.25, 12.50, and 25  $\mu$ g/mL. A linear relationship between absorbance and fisetin concentrations, as expected from Beer–Lambert's law, was verified for both standard ranges with the coefficient of determination  $R^2 = 0.9985$  and  $0.9984$ , respectively.

**5.9. Ethical and Animal Management.** Before any experiment, a dedicated protocol was examined and approved by the Animal Care Committee of the University Paris Descartes (project agreement 17-093, APAFIS N°2018031514511875) for each of the experiments in this study. Animals were housed, kept, and held according to the guidelines for ethical behavior established by the European Communities Council Directive (animal breeding agreement C92-049-01). Any signs of pain or discomfort were daily checked and minimized as much as possible. C57bl6 mice, coming from the approved breeding company Janvier Labs (Le Genest Saint Isle, France), were housed in the animal facility of the Department of Orofacial pathologies, imagery and biotherapies of Descartes University, Montrouge, France. Animals were kept at a temperature of  $22 \pm 2$  °C with a daily cyclical alternation of 12 h day and 12 h night. Animals had ad libitum access to standard breeding food and fresh tap water.

**5.10. Surgical Implantation, Experimental Procedure, and Sampling.** The surgical procedure has previously been detailed and described.<sup>32</sup> Briefly, C57bl6 mice (12 weeks old, ~30 g) were first anesthetized using a mixture of ketamine (80 mg/kg) and xylazine (10 mg/kg), both from Centravet Alfort, Maisons-Alfort, France, injected by an intraperitoneal route. After incision of the scalp skin, the periosteum was gently discarded to expose the animal skull. Then, a tissue punch (from Praxis l'Instrumentiste, France), mounted to a slow-speed handpiece operating at 1500 rpm, was used to create, on each side of the parietal bone, a 3.5 mm diameter calvaria critical-sized defect under irrigation with sterile saline solution. A sagittal suture was preserved, and the dura mater was

minimally damaged. Finally, the circular-drilled bone plug was gently extracted and removed, and each of the defects was either filled with a BG–PCL scaffold or a BG–PCL–Fis scaffold or else remained empty. Each of the implanted cylindrical scaffolds was of 3.5 mm diameter and 1 mm height ( $n = 4$  animals per group; 2 defects per animal,  $n = 8$  defects in total per group). The same type of scaffold was implanted in both defects within each animal. Special attention was taken to place each scaffold so that their cortical part faced the meninges. The negative control group for the critical-size defect was composed of six additional mice where each of the created defects was left empty. Finally, the skull skin was sutured using absorbable sutures (Vicryl Rapid 4.0, Ethicon, Johnson & Johnson), and postoperative analgesia was achieved by buprenorphine injection (0.02 mg/kg b.w.). After surgery, each operated animal was individually housed and constant observation was observed. No lethality was registered neither during the surgery nor during the postoperative time. Either infection or material exposure or other complication was reported during the whole wound healing progress. Body weights were daily recorded to guarantee appropriate feeding before and after the surgical procedure. On days 0, 30, 60, and 90 postsurgery, the skulls of each animal were *in vivo* imaged by X-ray microcomputed tomography (micro-CT), as explained below. On day 90, all animals were finally euthanized to excise their calvaria. Ethanol 70% v/v was used to fix samples (24 h at 4 °C). Then, graded ethanol solutions were used to gradually dehydrate the samples. Finally, each sample was embedded in methyl methacrylate resin (Merck) at  $-20^{\circ}$  without decalcification. Calvaria bone samples thus embedded into resin were cut (5  $\mu\text{m}$  thick) using a Jung Polycut E microtome (Leica) with hard tissue blades (Leica). Sections were sequentially immersed into a drop of 50% v/v ethanol, then stretched to a fold-free state on gelatin-coated glass slides (Menzel-Gläser), wrapped with a polyethylene sheet, finally pressed tightly on the glass, and allowed to dry overnight at room temperature. 2-Methoxyethyl acetate (Carlo Erba) was used to perform deplastification three times for 20 min, and graded ethanol solutions were used to rehydrate sections for subsequent processes.

**5.11. Microcomputed Tomography (Micro-CT).** At baseline, day 30, day 60, and day 90, mice were anesthetized using isoflurane (induction at 3–4% with an airflow of 0.8–1.5 L/min; 1.5–2% under 400–800 mL/min subsequently), and they were imaged using an X-ray micro-CT *in vivo* machine (Quantum FX Caliper, Life Sciences, Perkin Elmer, Waltham, MA) at Platform EA2496, Montrouge, France. The apparatus was set at 90 kV, 160  $\mu\text{A}$ , and an isotropic voxel size of 20  $\mu\text{m}$ . The scale bone density was daily calibrated using a dedicated internal density phantom. Full 3D high-resolution raw data were acquired (3 min scanning time) by spinning  $360^{\circ}$  around the sample both the flat panel detector and the X-ray electrical source. Open-source OsiriX imaging software (v5.7.1, distributed under LGPL license, Dr A. Rosset, Geneva, Switzerland) was used to perform tridimensional regions of interest from Dicom data frames. CTscan Analyzer software (Skyscan, release 1.13.5.1, Kontich, Belgium) was used to analyze and quantify the regenerated bone tissue inside each defect from each group. The initial defect area was isolated by drawing two-dimensional (2D) regions of interest on consecutive sections, and a global 3D volume of interest (VOI) was finally extracted from each sample by interpolation. The thus-extracted interpolated VOI contained only the remodeled

bone defect area. Bone material was then highlighted interactively using a global threshold, thus eliminating the background noise. “New-formed tissue” volumetric ratios were extracted comparatively to the total volume of the initial defect.

**5.12. Histological Examination of Samples.** Sections (5  $\mu\text{m}$  thick) of deplastified calvaria bone samples were sequentially stained with modified Masson–Goldner trichrome or processed for alkaline phosphatase (ALP) and tartrate-resistant acid phosphatase (TRAP) by enzyme histochemistry. Modified Masson–Goldner trichrome staining allowed visualizing the osteoid and mineralized bone tissues. TRAP was detected by hexazotized pararosanilin and naphthol AS-TR phosphate (both from Sigma-Aldrich, St. Louis, MO) to reveal osteoclasts; nonosteoclastic acid phosphatase was inhibited by adding 100 mMol/L of L(+)-tartaric acid (Sigma) to the substrate solution. Image acquisition was performed using a DMLB Leica microscope, equipped with an imaging camera DFC425 Leica connected to the Leica application (LAS version 4.4).

**5.13. Statistics.** For each group, results were expressed as the mean value  $\pm$  standard deviation (SD). Analysis of variance (ANOVA) followed by two-way comparisons performed with Tukey’s HSD tests (ExcelStat Pro software, Microsoft Office 2007) was used to compare variables for *in vitro* assays. For *in vivo* experiments, values were compared using one-way analysis of variance (ANOVA) followed by two-way comparisons performed with paired Student’s *t*-test if they passed the Fisher *F* equal variance and Shapiro–Wilk normality tests. If not, they were compared using Kruskal–Wallis ANOVA test on the ranks followed by two-way comparison tests performed with the Mann–Whitney *U* test. Statistical results were considered significant when *p* was less than 0.05. Groups with significant differences ( $p < 0.05$ ) are indicated with different letters (a, b, c, d, e...).

## ■ ASSOCIATED CONTENT

### SI Supporting Information

The Supporting Information is available free of charge at <https://pubs.acs.org/doi/10.1021/acsomega.2c01109>.

Videos of  $\mu\text{-CT}$  analysis of the different scaffolds (BG–PCL, BG–PCL–Fis) implanted in critical-size mice calvaria defects compared to an empty (sham) control defect at 90 days (MP4)

BG–PCL-D90 (MP4)

BG–PCL–Fis-D90 (MP4)

## ■ AUTHOR INFORMATION

### Corresponding Author

Yohann Wittrant – INRAE, Human Nutrition Unit (UNH), ECREIN Team, TSA 50400, Clermont-Ferrand, Auvergne-Rhône-Alpes 63001, France; [orcid.org/0000-0003-3811-8859](https://orcid.org/0000-0003-3811-8859); Email: [yohann.wittrant@inrae.fr](mailto:yohann.wittrant@inrae.fr)

### Authors

Henri Granel – INRAE, Human Nutrition Unit (UNH), ECREIN Team, TSA 50400, Clermont-Ferrand, Auvergne-Rhône-Alpes 63001, France

Cédric Bossard – Université Clermont Auvergne, Laboratoire De Physique De Clermont Ferrand, Clermont-Ferrand, Auvergne-Rhône-Alpes 63001, France; [orcid.org/0000-0002-7892-1382](https://orcid.org/0000-0002-7892-1382)

Anne-Margaux Collignon – Descartes University of Paris Faculty of Dental Surgery, Laboratoires Pathologies, Imagerie et Biothérapies Orofaciales, Montrouge, Île-De-France 92120, France

Fabien Wauquier – INRAE, Human Nutrition Unit (UNH), ECREIN Team, TSA 50400, Clermont-Ferrand, Auvergne-Rhône-Alpes 63001, France

Julie Lesieur – Descartes University of Paris Faculty of Dental Surgery, Laboratoires Pathologies, Imagerie et Biothérapies Orofaciales, Montrouge, Île-De-France 92120, France

Gael Y. Rochefort – Descartes University of Paris Faculty of Dental Surgery, Laboratoires Pathologies, Imagerie et Biothérapies Orofaciales, Montrouge, Île-De-France 92120, France

Edouard Jallot – Université Clermont Auvergne, Laboratoire De Physique De Clermont Ferrand, Clermont-Ferrand, Auvergne-Rhône-Alpes 63001, France

Jonathan Lao – Université Clermont Auvergne, Laboratoire De Physique De Clermont Ferrand, Clermont-Ferrand, Auvergne-Rhône-Alpes 63001, France

Complete contact information is available at:

<https://pubs.acs.org/10.1021/acsomega.2c01109>

## Notes

The authors declare no competing financial interest.

## ACKNOWLEDGMENTS

The authors thank Dr. Brigitte Gaillard Martinie, the Plateau Technique de Microscopie du Centre INRA ARA (UMR 454, MEDIS), and the Centre Imagerie Cellulaire Santé (CICS – Faculté de Médecine de Clermont-Ferrand) for SEM imaging of cells on biomaterials; Professor Catherine Chaussain and the Laboratoires Pathologies, Imagerie et Biothérapies orofaciales (EA2496), for the access to the animal facility; OST Développement (Clermont-Ferrand, France) for providing the Lubbock and cortical bone samples and for carrying out the sterilization of the materials; and the Polytech Clermont School of Engineering Physics for spectrophotometry measurements. The project was supported by the “Fonds Européen de Développement Régional” (FEDER) and Région Auvergne-Rhône-Alpes under the “pack Ambition Recherche” and “Thématiques Emergentes” programs.

## REFERENCES

- (1) (a) Chevalier, J.; Gremillard, L. New Trends in Ceramics for Orthopedics. In *Encyclopedia of Materials: Science and Technology*; Elsevier, 2007; pp 1–8. (b) Granel, H.; Bossard, C.; Nucke, L.; Wauquier, F.; Rochefort, G. Y.; Guicheux, J.; Jallot, E.; Lao, J.; Wittrant, Y. Optimized Bioactive Glass: the Quest for the Bony Graft. *Adv. Healthcare Mater.* **2019**, *8*, No. 1801542.
- (2) Baino, F.; Novajra, G.; Vitale-Brovarone, C. Bioceramics and Scaffolds: A Winning Combination for Tissue Engineering. *Front. Bioeng. Biotechnol.* **2015**, *3*, No. 202.
- (3) Jones, J. R. Review of bioactive glass: from Hench to hybrids. *Acta Biomater.* **2013**, *9*, 4457–4486.
- (4) (a) Bossard, C.; Granel, H.; Wittrant, Y.; Jallot, E.; Lao, J.; Vial, C.; Tiainen, H. Polycaprolactone / bioactive glass hybrid scaffolds for bone regeneration. *Biomed. Glasses* **2018**, *4*, 108–122. (b) Hendriks, S.; Kascholke, C.; Flath, T.; Schumann, D.; Gressenbuch, M.; Schulze, F. P.; Hacker, M. C.; Schulz-Siegmund, M. Indirect rapid prototyping of sol-gel hybrid glass scaffolds for bone regeneration - Effects of organic crosslinker valence, content and molecular weight on mechanical properties. *Acta Biomater.* **2016**, *35*, 318–329. (c) Lao, J.; Dieudonné, X.; Fayon, F.; Montouillout, V.; Jallot, E. Bioactive glass–gelatin hybrids: building scaffolds with enhanced calcium incorporation and controlled porosity for bone regeneration. *J. Mater. Chem. B* **2016**, *4*, 2486–2497. (d) Mondal, D.; Rizkalla, A. S.; Mequanint, K. Bioactive borophosphosilicate-polycaprolactone hybrid biomaterials via a non-aqueous sol gel process. *RSC Adv.* **2016**, *6*, 92824–92832. (e) Tallia, F.; Russo, L.; Li, S.; Orrin, A. L. H.; Shij, X.; Chen, S.; Steele, J. A. M.; Meille, S.; Chevalier, J.; Lee, P. D.; Stevens, M. M.; Cipolla, L.; Jones, J. R. Bouncing and 3D printable hybrids with self-healing properties. *Mater. Horiz.* **2018**, *5*, 849–860.
- (5) (a) Trimmel, B.; Gede, N.; Hegyi, P.; Szakacs, Z.; Mezey, G. A.; Varga, E.; Kivovics, M.; Hanak, L.; Rumbus, Z.; Szabo, G. Relative performance of various biomaterials used for maxillary sinus augmentation: A Bayesian network meta-analysis. *Clin. Oral Implants Res.* **2021**, *32*, 135–153. (b) Athanasiou, V. T.; Papachristou, D. J.; Panagopoulos, A.; Saridis, A.; Scopra, C. D.; Megas, P. Histological comparison of autograft, allograft-DBM, xenograft, and synthetic grafts in a trabecular bone defect: an experimental study in rabbits. *Med. Sci. Monit.* **2009**, *16*, BR24–BR31. (c) Granel, H.; Bossard, C.; Collignon, A.-M.; Wauquier, F.; Lesieur, J.; Rochefort, G. Y.; Jallot, E.; Lao, J.; Wittrant, Y. Bioactive Glass/Polycaprolactone Hybrid with a Dual Cortical/Trabecular Structure for Bone Regeneration. *ACS Appl. Bio Mater.* **2019**, *2*, 3473–3483. (d) Le Meng Bao, C.; Teo, E. L.; Chong, M. S. K.; Liu, Y.; Choolani, M.; Chan, J. K. Y. Advances in Bone Tissue Engineering. In *Regenerative Medicine and Tissue Engineering*, Andrades, J. A., Ed.; InTech, 2013.
- (6) (a) Aghali, A. Craniofacial Bone Tissue Engineering: Current Approaches and Potential Therapy. *Cells* **2021**, *10*, No. 2993. (b) Ishack, S.; Mediero, A.; Wilder, T.; Ricci, J. L.; Cronstein, B. N. Bone regeneration in critical bone defects using three-dimensionally printed  $\beta$ -tricalcium phosphate/hydroxyapatite scaffolds is enhanced by coating scaffolds with either dipyrindamole or BMP-2. *J. Biomed. Mater. Res., Part B* **2017**, *105*, 366–375. (c) Jung, R. E.; Windisch, S. I.; Eggenschwiler, A. M.; Thoma, D. S.; Weber, F. E.; Hämmerle, C. H. F. A randomized-controlled clinical trial evaluating clinical and radiological outcomes after 3 and 5 years of dental implants placed in bone regenerated by means of GBR techniques with or without the addition of BMP-2. *Clin. Oral Implants Res.* **2009**, *20*, 660–666. (d) Kim, H. J.; Chung, J. H.; Shin, S. Y.; Shin, S. I.; Kye, S. B.; Kim, N. K.; Kwon, T. G.; Paeng, J. Y.; Kim, J. W.; Oh, O. H.; Kook, M. S.; Yang, H. J.; Hwang, S. J. Efficacy of rhBMP-2/Hydroxyapatite on Sinus Floor Augmentation: A Multicenter, Randomized Controlled Clinical Trial. *J. Dent. Res.* **2015**, *94*, 158S–65S. (e) Lieberman, J. R.; Daluiski, A.; Einhorn, T. A. The role of growth factors in the repair of bone. Biology and clinical applications. *J. Bone Jt. Surg., Am. Vol.* **2002**, *84*, 1032–1044. (f) Mehta, M.; Schmidt-Bleek, K.; Duda, G. N.; Mooney, D. J. Biomaterial delivery of morphogens to mimic the natural healing cascade in bone. *Adv. Drug Delivery Rev.* **2012**, *64*, 1257–1276. (g) Nam, J. W.; Khureltohtokh, S.; Choi, H. M.; Lee, A. R.; Park, Y. B.; Kim, H. J. Randomised controlled clinical trial of augmentation of the alveolar ridge using recombinant human bone morphogenetic protein 2 with hydroxyapatite and bovine-derived xenografts: comparison of changes in volume. *Br. J. Oral Maxillofac. Surg.* **2017**, *55*, 822–829. (h) Oryan, A.; Alidadi, S.; Moshiri, A.; Bigham-Sadegh, A. Bone morphogenetic proteins: a powerful osteoinductive compound with non-negligible side effects and limitations. *BioFactors* **2014**, *40*, 459–481. (i) Tsuzuki, N.; Otsuka, K.; Seo, J.; Yamada, K.; Haneda, S.; Furuoka, H.; Tabata, Y.; Sasaki, N. In vivo osteoinductivity of gelatin  $\beta$ -tri-calcium phosphate sponge and bone morphogenetic protein-2 on an equine third metacarpal bone defect. *Res. Vet. Sci.* **2012**, *93*, 1021–1025. (j) Wang, T.; Guo, S.; Zhang, H. Synergistic Effects of Controlled-Released BMP-2 and VEGF from nHAC/PLGA Scaffold on Osteogenesis. *BioMed Res. Int.* **2018**, *2018*, 1–12.
- (7) (a) Carragee, E. J.; Chu, G.; Rohatgi, R.; Hurwitz, E. L.; Weiner, B. K.; Yoon, S. T.; Comer, G.; Kopjar, B. Cancer risk after use of recombinant bone morphogenetic protein-2 for spinal arthrodesis. *J. Bone Jt. Surg.* **2013**, *95*, 1537–1545. (b) Crandall, D. G.; Revella, J.; Patterson, J.; Huish, E.; Chang, M.; McLemore, R. Transforaminal

- lumbar interbody fusion with rhBMP-2 in spinal deformity, spondylolisthesis, and degenerative disease—part 1: Large series diagnosis related outcomes and complications with 2- to 9-year follow-up. *Spine* **2013**, *38*, 1128–1136. (c) Marx, R. E.; Armentano, L.; Olavarria, A.; Samaniego, J. rhBMP-2/ACS grafts versus autogenous cancellous marrow grafts in large vertical defects of the maxilla: an unsponsored randomized open-label clinical trial. *Int. J. Oral Maxillofac. Implants* **2013**, *28*, e243–251. (d) Singh, K.; Nandyala, S. V.; Marquez-Lara, A.; Cha, T. D.; Khan, S. N.; Fineberg, S. J.; Pelton, M. A. Clinical sequelae after rhBMP-2 use in a minimally invasive transforaminal lumbar interbody fusion. *Spine J.* **2013**, *13*, 1118–1125.
- (8) (a) Murgia, D.; Mauceri, R.; Campisi, G.; De Caro, V. Advance on Resveratrol Application in Bone Regeneration: Progress and Perspectives for Use in Oral and Maxillofacial Surgery. *Biomolecules* **2019**, *9*, No. 94. (b) Hubert, P. A.; Lee, S. G.; Lee, S.-K.; Chun, O. K. Dietary Polyphenols, Berries, and Age-Related Bone Loss: A Review Based on Human, Animal, and Cell Studies. *Antioxidants* **2014**, *3*, 144–158. (c) Nicolini, V.; De Tommasi, N.; Nori, S. L.; Costantinides, F.; Berton, F.; Di Lenarda, R. Modulatory Effects of Plant Polyphenols on Bone Remodeling: A Prospective View From the Bench to Bedside. *Front. Endocrinol.* **2019**, *10*, No. 494.
- (9) (a) Cerqueni, G.; Scalzone, A.; Licini, C.; Gentile, P.; Mattioli-Belmonte, M. Insights into oxidative stress in bone tissue and novel challenges for biomaterials. *Mater. Sci. Eng., C* **2021**, *130*, No. 112433. (b) Awale, G.; Wong, E.; Rajpura, K.; Lo, K. W.-H. Engineered Bone Tissue with Naturally-Derived Small Molecules. *Curr. Pharm. Des.* **2017**, *23*, 3585–3594. (c) Shavandi, A.; El-Din Ahmed Bekhit, A.; Saeedi, P.; Izadifar, Z.; Bekhit, A. A.; Khademhosseini, A. Polyphenol uses in biomaterials engineering. *Biomaterials* **2018**, *167*, 91–106.
- (10) (a) Fernández-Villa, D.; Gómez-Lavín, M. J.; Abradelo, C.; Román, J. S.; Rojo, L. Tissue Engineering Therapies Based on Folic Acid and Other Vitamin B Derivatives. Functional Mechanisms and Current Applications in Regenerative Medicine. *Int. J. Mol. Sci.* **2018**, *19*, No. 4068. (b) Saveleva, M. S.; Ivanov, A. N.; Kurtukova, M. O.; Atkin, V. S.; Ivanova, A. G.; Lyubun, G. P.; Martuyukova, A. V.; Cherevko, E. I.; Sargsyan, A. K.; Fedonnikov, A. S.; Norkin, I. A.; Skirtach, A. G.; Gorin, D. A.; Parakhonskiy, B. V. Hybrid PCL/CaCO<sub>3</sub> scaffolds with capabilities of carrying biologically active molecules: Synthesis, loading and in vivo applications. *Mater. Sci. Eng., C* **2018**, *85*, 57–67. (c) Cao, Z.; Wang, D.; Lyu, L.; Gong, Y.; Li, Y. Fabrication and characterization of PCL/CaCO<sub>3</sub> electrospun composite membrane for bone repair. *RSC Adv.* **2016**, *6*, 10641–10649.
- (11) (a) Yao, Y.; Zhang, H.; Wang, Z.; Ding, J.; Wang, S.; Huang, B.; Ke, S.; Gao, C. Reactive oxygen species (ROS)-responsive biomaterials mediate tissue microenvironments and tissue regeneration. *J. Mater. Chem. B* **2019**, *7*, 5019–5037. (b) Bonifacio, M. A.; Cerqueni, G.; Cometa, S.; Licini, C.; Sabbatini, L.; Mattioli-Belmonte, M.; De Giglio, E. Insights into Arbutin Effects on Bone Cells: Towards the Development of Antioxidant Titanium Implants. *Antioxidants* **2020**, *9*, No. 579.
- (12) Leotoing, L.; Wauquier, F.; Guicheux, J.; Miot-Noirault, E.; Wittrant, Y.; Coxam, V. The polyphenol fisetin protects bone by repressing NF- $\kappa$ B and MKP-1-dependent signaling pathways in osteoclasts. *PLoS One* **2013**, *8*, No. e68388.
- (13) Léotoing, L.; Davicco, M.-J.; Lebecque, P.; Wittrant, Y.; Coxam, V. The flavonoid fisetin promotes osteoblast differentiation through Runx2 transcriptional activity. *Mol. Nutr. Food Res.* **2014**, *58*, 1239–1248.
- (14) Molagoda, I. M. N.; Kang, C. H.; Lee, M. H.; Choi, Y. H.; Lee, C. M.; Lee, S.; Kim, G. Y. Fisetin promotes osteoblast differentiation and osteogenesis through GSK-3 $\beta$  phosphorylation at Ser9 and consequent beta-catenin activation, inhibiting osteoporosis. *Biochem. Pharmacol.* **2021**, *192*, No. 114676.
- (15) (a) Fu, C. Y.; Chen, M. C.; Tseng, Y. S.; Chen, M. C.; Zhou, Z.; Yang, J. J.; Lin, Y. M.; Viswanatha, V. P.; Wang, G.; Huang, C. Y. Fisetin activates Hippo pathway and JNK/ERK/AP-1 signaling to inhibit proliferation and induce apoptosis of human osteosarcoma cells via ZAK overexpression. *Environ. Toxicol.* **2019**, *34*, 902–911. (b) Xing, C.; Zhang, Y.; Su, R.; Wu, R. Anticancer activity of Fisetin against the human osteosarcoma cell lines involves G2/M cell cycle arrest, mitochondrial apoptosis and inhibition of cell migration and invasion. *J. BUON* **2020**, *25*, 1022–1027.
- (16) Gritsch, L.; Granel, H.; Charbonnel, N.; Jallot, E.; Wittrant, Y.; Forestier, C.; Lao, J. Tailored therapeutic release from polycaprolactone-silica hybrids for the treatment of osteomyelitis: antibiotic rifampicin and osteogenic silicates. *Biomater. Sci.* **2022**, *10*, 1936–1951.
- (17) (a) Olivier, F.; Bonnamy, S.; Rochet, N.; Drouet, C. Activated Carbon Fiber Cloth/Biomimetic Apatite: A Dual Drug Delivery System. *Int. J. Mol. Sci.* **2021**, *22*, No. 12247. (b) Li, F.; Wu, W.; Xiang, L.; Hong, H.; Jiang, H.; Qian, J.; Weng, G. Sustained release of VH and rhBMP-2 from nanoporous magnesium-zinc-silicon xerogels for osteomyelitis treatment and bone repair. *Int. J. Nanomed.* **2015**, *10*, 4071–4080. (c) Kim, E.-C.; Lim, H.-C.; Nam, O. H.; Kim, M.-j.; El-Fiqi, A.; Yun, H.-M.; Lee, Y.-M.; Jin, G.-Z.; Lee, H.-H.; Kim, H.-W. Delivery of dexamethasone from bioactive nanofiber matrices stimulates odontogenesis of human dental pulp cells through integrin/BMP/mTOR signaling pathways. *Int. J. Nanomed.* **2016**, *11*, 2557–2567. (d) Tang, W.; Lin, D.; Yu, Y.; Niu, H.; Guo, H.; Yuan, Y.; Liu, C. Bioinspired trimodal macro/micro/nano-porous scaffolds loading rhBMP-2 for complete regeneration of critical size bone defect. *Acta Biomater.* **2016**, *32*, 309–323. (e) Wu, C.; Fan, W.; Chang, J.; Xiao, Y. Mesoporous bioactive glass scaffolds for efficient delivery of vascular endothelial growth factor. *J. Biomater. Appl.* **2013**, *28*, 367–374.
- (18) Bossard, C.; Granel, H.; Jallot, É.; Montouillout, V.; Fayon, F.; Soulié, J.; Drouet, C.; Wittrant, Y.; Lao, J. Mechanism of Calcium Incorporation Inside Sol–Gel Silicate Bioactive Glass and the Advantage of Using Ca(OH)<sub>2</sub> over Other Calcium Sources. *ACS Biomater. Sci. Eng.* **2019**, *5*, 5906–5915.
- (19) (a) Biondi, M.; Ungaro, F.; Quaglia, F.; Netti, P. A. Controlled drug delivery in tissue engineering. *Adv. Drug Delivery Rev.* **2008**, *60*, 229–242. (b) Cazzola, M.; Corazzari, I.; Prenesti, E.; Bertone, E.; Vernè, E.; Ferraris, S. Bioactive glass coupling with natural polyphenols: Surface modification, bioactivity and anti-oxidant ability. *Appl. Surf. Sci.* **2016**, *367*, 237–248.
- (20) (a) Bruschi, M. L. *Strategies to Modify the Drug Release from Pharmaceutical Systems*; Elsevier Science: San Diego, CA, 2015. (b) Mulye, N. V.; Turco, S. J. A Simple Model Based on First Order Kinetics to Explain Release of Highly Water Soluble Drugs from Porous Dicalcium Phosphate Dihydrate Matrices. *Drug Dev. Ind. Pharm.* **1995**, *21*, 943–953.
- (21) Lim, J.; Lee, J.; Yun, H.-S.; Shin, H.-I.; Park, E. K. Comparison of bone regeneration rate in flat and long bone defects: Calvarial and tibial bone. *Tissue Eng. Regen. Med.* **2013**, *10*, 336–340.
- (22) Gu, Y.; Huang, W.; Rahaman, M. N.; Day, D. E. Bone regeneration in rat calvarial defects implanted with fibrous scaffolds composed of a mixture of silicate and borate bioactive glasses. *Acta Biomater.* **2013**, *9*, 9126–9136.
- (23) Gronowicz, G.; Jacobs, E.; Peng, T.; Zhu, L.; Hurley, M.; Kuhn, L. T. Calvarial Bone Regeneration Is Enhanced by Sequential Delivery of FGF-2 and BMP-2 from Layer-by-Layer Coatings with a Biomimetic Calcium Phosphate Barrier Layer. *Tissue Eng., Part A* **2017**, *23*, 1490–1501.
- (24) Reyes, R.; Rodríguez, J. A.; Orbe, J.; Arnau, M. R.; Évora, C.; Delgado, A. Combined sustained release of BMP2 and MMP10 accelerates bone formation and mineralization of calvaria critical size defect in mice. *Drug Delivery* **2018**, *25*, 750–756.
- (25) Samsonraj, R. M.; Dudakovic, A.; Zan, P.; Pichurin, O.; Cool, S. M.; van Wijnen, A. J. A Versatile Protocol for Studying Calvarial Bone Defect Healing in a Mouse Model. *Tissue Eng., Part C* **2017**, *23*, 686–693.
- (26) (a) Cowan, C. M.; Aghaloo, T.; Chou, Y.-F.; Walder, B.; Zhang, X.; Soo, C.; Ting, K.; Wu, B. MicroCT evaluation of three-dimensional mineralization in response to BMP-2 doses in vitro and in critical sized rat calvarial defects. *Tissue Eng.* **2007**, *13*, 501–512.

(b) Lin, C.-Y.; Chang, Y.-H.; Li, K.-C.; Lu, C.-H.; Sung, L.-Y.; Yeh, C.-L.; Lin, K.-J.; Huang, S.-F.; Yen, T.-C.; Hu, Y.-C. The use of ASCs engineered to express BMP2 or TGF- $\beta$ 3 within scaffold constructs to promote calvarial bone repair. *Biomaterials* **2013**, *34*, 9401–9412.

(27) Ma, Z.; Gao, C.; Gong, Y.; Shen, J. Paraffin spheres as porogen to fabricate poly(L-lactic acid) scaffolds with improved cytocompatibility for cartilage tissue engineering. *J. Biomed. Mater. Res.* **2003**, *67B*, 610–617.

(28) (a) Bellows, C. G.; Aubin, J. E.; Heersche, J. N. M. Initiation and progression of mineralization of bone nodules formed in vitro: the role of alkaline phosphatase and organic phosphate. *Bone Miner.* **1991**, *14*, 27–40. (b) Bellows, C. G.; Aubin, J. E.; Heersche, J. N. M.; Antosz, M. E. Mineralized bone nodules formed in vitro from enzymatically released rat calvaria cell populations. *Calcif. Tissue Int.* **1986**, *38*, 143–154. (c) Ishida, H.; Bellows, C. G.; Aubin, J. E.; Heersche, J. N. Characterization of the 1,25-(OH) $_2$ D $_3$ -induced inhibition of bone nodule formation in long-term cultures of fetal rat calvaria cells. *Endocrinology* **1993**, *132*, 61–66.

(29) Radin, S.; Ducheyne, P.; Rothman, B.; Conti, A. The effect of in vitro modeling conditions on the surface reactions of bioactive glass. *J. Biomed. Mater. Res.* **1997**, *37*, 363–375.

(30) Wu, S.-C. Influence of hydrodynamic shear stress on microcarrier-attached cell growth: Cell line dependency and surfactant protection. *Bioprocess Eng.* **1999**, *21*, 201–206.

(31) Perez, R. A.; Riccardi, K.; Altankov, G.; Ginebra, M.-P. Dynamic cell culture on calcium phosphate microcarriers for bone tissue engineering applications. *J. Tissue Eng.* **2014**, *5*, No. 204173141454396.

(32) Collignon, A. M.; Lesieur, J.; Anizan, N.; Azzouna, R. B.; Poliard, A.; Gorin, C.; Letourneur, D.; Chaussain, C.; Rouzet, F.; Rochefort, G. Y. Early angiogenesis detected by PET imaging with  $^{64}\text{Cu}$ -NODAGA-RGD is predictive of bone critical defect repair. *Acta Biomater.* **2018**, *82*, 111–121.